hydrogen

MDPI

Article

First-Principles Investigation of Structural, Electronic, Thermoelectric, and Hydrogen Storage Properties of Mg*X*H$_3$ (X = Cr, Mn, Fe, Co, Ni, Cu) Perovskite Hydrides

Ayoub Koufi [1,2], Younes Ziat [1,2] and Hamza Belkhanchi [1,2,*]

[1] Engineering and Applied Physics Team (EAPT), Superior School of Technology, Sultan Moulay Slimane University, Beni Mellal 23000, Morocco

[2] The Moroccan Association of Sciences and Techniques for Sustainable Development, Beni Mellal 23000, Morocco

* Correspondence: hamzastudentestbm@gmail.com

Abstract

This paper is based on the BoltzTrap package implemented in the Wien2k code to theoretically analyze and predict the structural, electronic, thermoelectric, and hydrogen storage properties of Mg*X*H$_3$ hydride perovskites (X = Cr, Mn, Fe, Co, Ni, and Cu). The study explores the dual functional potential of these compounds, highlighting how their hydrogen storage capability relates to their temperature-dependent thermoelectric performance. Analysis of band structures and densities of electronic states (DOS) reveals that all the compounds studied exhibit metallic behavior, characterized by an overlap between the valence band and the conduction band, indicating a zero electronic gap. Thermal properties show great variability depending on the transition metal involved. In particular, electrical conductivity and thermal conductivity evolve differently with temperature, directly influencing the figure of merit (Zt) of thermoelectric materials. The results suggest that although most Mg*X*H$_3$ compounds are not promising candidates for thermoelectric applications due to their high thermal conductivity and low density of states near the E_F, MgNiH$_3$ and MgCuH$_3$ stand out with attractive thermoelectric potential. These properties make them attractive for energy conversion, waste heat recovery and solid-state cooling applications. This theoretical study highlights the potential of magnesium-based perovskite hydrides in energy conversion technologies, including thermoelectricity and hydrogen storage.

Keywords: BoltzTrap; electrical conductivity; Mg*X*H$_3$ perovskite hydrides; thermal conductivity; Seebeck coefficient

check for updates

Academic Editor: Thi Thu Le

Received: 29 September 2025
Revised: 25 October 2025
Accepted: 3 November 2025
Published: 11 November 2025

Citation: Koufi, A.; Ziat, Y.; Belkhanchi, H. First-Principles Investigation of Structural, Electronic, Thermoelectric, and Hydrogen Storage Properties of Mg*X*H$_3$ (X = Cr, Mn, Fe, Co, Ni, Cu) Perovskite Hydrides. *Hydrogen* **2025**, *6*, 106. https://doi.org/10.3390/hydrogen6040106

1. Introduction

The hydrogen energy chain encompasses production, storage, and transportation processes, making it a key component of future sustainable energy systems. However, hydrogen storage remains a major challenge [1,2], requiring significant technological advances before widespread adoption is possible [3,4]. Growing energy demand, mainly due to population growth and industrialization, has led to excessive consumption of fossil fuels. This increased dependence has led to a critical rise in carbon dioxide levels, exacerbating global warming and other environmental problems. To meet these challenges, various alternative energy sources, including hydrogen, wind, nuclear and solar power, are being explored to reduce dependence on fossil fuels and mitigate their environmental impacts [5–7].

The enhancement of natural resources and the increase in gas emissions create a warming effect, which accelerates climate change. To remedy this, the importance of green energies is emphasized, especially green hydrogen, which is produced by electrolysis of water with the help of renewable energies. Thus, a historical and technical overview of hydrogen has been provided, where current production methods are explored [8]. Nevertheless, hydrogen storage and transportation remain major obstacles to its large-scale integration into the energy mix [7,9,10]. Due to its CO_2-emission-free production, high energy efficiency, and abundance in the environment, hydrogen is attracting growing interest as a clean and sustainable energy carrier [11–13].

Solid-state hydrogen storage represents a promising approach thanks to its high capacity, reversibility and relatively affordable cost, notably using magnesium hydrides [1,14]. However, its practical application is limited by technical challenges such as slow reaction kinetics and high operating temperatures [3,14]. Consequently, optimizing the performance of magnesium hydrides remains a key objective of ongoing research [15]. Although it sometimes comes at the expense of storage capacity, the inclusion of transition metal dopants has been investigated to enhance hydrogen absorption and desorption rates [16].

In this context, DFT is emerging as the tool of choice for studying the electronic and structural properties of hydrogen storage [17–21]. This quantum simulation approach makes it possible to accurately describe the ground state of N-body systems, whether atoms, molecules or condensed phases, using functionals adapted to the electron density [22–24]. Thanks to advances in computational methods and improvements in the approximations used, DFT is now an indispensable tool in theoretical chemistry and materials science, despite certain intrinsic limitations [25–28].

The aim of this study is to highlight the growing interest in perovskite-type hydrides as hydrogen storage materials, highlighting their remarkable properties and their potential in the development of new energy solutions [29,30]. Experimental work has already explored the use of $NaMgH_3$ hydrides for reversible hydration and dehydration processes [31]. In addition, studies have been carried out on the synthesis of $NaMgH_3$ and $KMgH_3$ at high pressure and high temperature to assess their stability and storage capacity [32]. Other compositions such as $KCuH_3$, $SrPdH_3$, $CaNiH_3$, $CaCoH_3$, $MgCuH_3$, $MgCoH_3$, $MgFeH_3$, $MgCrH_3$, $LiFeH_3$ and $LiCuH_3$ have also been examined for their potential in hydrogen storage [33–36]. In addition, we have selected several alkali and alkaline earth hydrides, including $NaMnH_3$, $CsCaH_3$, $RbCaH_3$, $KCaH_3$, $KMgH_3$, $CsMgH_3$, $BaLiH_3$ and $SrLiH_3$, which have been the subject of recent investigations [37,38].

Using DFT we have explored the electronic and thermoelectric nature of $MgXH_3$ (X = Cr, Mn, Fe, Co, Ni, and Cu) in this study. The next sections describe the computational methodology used, show the results that we obtained, and discuss them. In addition, this study has also employed the BoltzTraP code, integrated into the DFT calculations, to explore the temperature dependence of the thermoelectric properties, a crucial parameter to evaluate their performance as hydrogen storage materials.

Therefore, this work aims to provide a comprehensive theoretical understanding of $MgXH_3$ perovskite hydrides by jointly evaluating their hydrogen storage characteristics and thermoelectric behavior. These two aspects are interrelated, as the hydrogen content and electronic structure directly influence the transport and energetic performance of these materials. Such a dual approach allows identifying promising multifunctional hydrides that could serve both as hydrogen storage media and as components in energy conversion systems.

2. Calculation Method

GGA was applied in this study to theoretically analyze the hydrogen storage capacity and the structural, electronic and thermoelectric properties of MgXH$_3$ (where X can be Cr, Mn, Fe, Co, Ni and Cu). These analyses were done in the context of DFT, which allows for the interaction and correlation effects of these systems to be well defined. The Wien2k code was used to perform the computations, based on the FP-LAPW method. To explore thermoelectric properties, the Seebeck coefficient and electronic conductivity as a function of temperature were measured using the BoltzTraP module [39]. Structural optimization was performed using the "Birch-Murnaghan equation of stat (EOS)", ensuring optimal convergence of crystal parameters. Calculation accuracy was ensured by setting the convergence tolerance of the self-consistent field (SCF) to 10^{-4} e for charge and 10^{-3} Ry for total energy. In addition, the Brillouin zone was sampled with a high k-point density (1000 points), adopting octahedral integration to ensure a fine description of the system's electronic properties.

3. Interpretation of Results

3.1. Structural Properties

A well-defined crystallographic arrangement characterizes the fundamental structure of the hydride perovskite MgXH$_3$. Magnesium atoms (Mg) occupy the elemental lattice vertices in (0, 0, 0), while X transition atoms are positioned in the center of the lattice in (1/2, 1/2, 1/2). (H) is located at face centers, with specific coordinates (0, 1/2, 1/2), (1/2, 0, 1/2) and (1/2, 1/2, 0) [40,41].

The crystal structure of perovskite-type hydrides adopts cubic symmetry with space group (no. 221). The lattice parameter of MgXH$_3$, presented in Table 1, validates the accuracy of the calculations and the consistency of the data obtained. This crystallographic configuration is in agreement with structures reported in the literature, as illustrated in Figure 1.

Table 1. Experimental, theoretical, and optimized lattice parameters ($a_0 = b_0 = c_0$, in Å) of MgXH$_3$ (X = Cr, Mn, Fe, Co, Ni, Cu) perovskite hydrides.

	Parameter ($a_0 = b_0 = c_0$)		
	Exp. Values (Å)	**Theoretical Values (Å)**	**Lattice Parameters Optimize (Å)**
$MgCrH_3$	3.45 [41]	3.4590 [41]	3.3807
$MgMnH_3$	3.34 [41]	3.3485 [41]	3.3199
$MgFeH_3$	3.02 [41]	3.0284 [41]	3.2958
$MgCoH_3$	3.31 [42]	3.278 [43]	3.2997
$MgNiH_3$	3.32 [44]	3.370 [42]	3.3572
$MgCuH_3$	3.32 [44]	3.456 [45]	3.4817

Geometric optimization is a crucial step in determining the fundamental properties of MgXH$_3$. The main objective is to minimize the total energy of the system as a function of geometrical parameters, including elemental mesh volume and c/a ratio, to obtain the most stable thermodynamic equilibrium configuration. This procedure is carried out in two phases. First, the internal forces acting on the atoms within the unit cell are calculated and successively reduced until they reach a negligible value, thus guaranteeing a stable mechanical state. Next, the total energy of the system is evaluated for different values of volume and c/a ratio to plot the energy–volume curve. The latter enables structural stability to be examined and the fundamental parameters of the compound to be extracted.

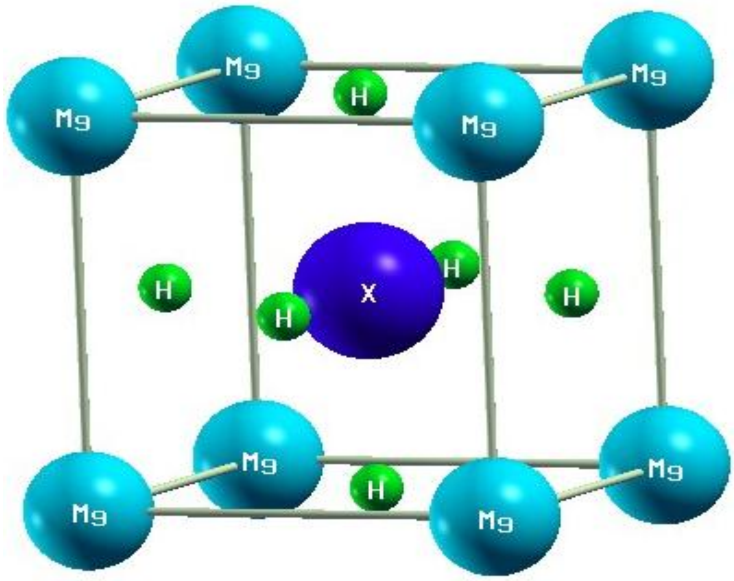

Figure 1. Structure of $MgXH_3$ (X = Cr, Mn, Fe, Co, Ni, and Cu).

The energy–volume relationship is fitted using the EOS, an approach widely used to model the compressible behavior of solids [46–48]:

$$E = E_0 + \frac{B_0}{B_0'}(V - V_0) - \frac{B_0 V_0}{B_0'(1 - B_0')}\left[\left(\frac{V}{V_0}\right)^{1-B_0'} - 1\right] \quad (1)$$

where E_0 represents the minimum energy corresponding to equilibrium volume V_0, B_0 is the modulus of compressibility and $B_0{}'$ is its derivative to pressure. The corresponding results are presented in Table 2.

Table 2. Calculated optimized parameters a_0, V, E, B and B′ of $MgXH_3$ (X = Cr, Mn, Fe, Co, Ni, Cu).

Compound	Lattice Parameters Optimize (Å)	Volume V (Å^3)	Total Energy E (Ry)	Bulk Modulus B (GPa)	Pressure Derivative B′
MgCrH3	3.3807	38.67	−2505.93726	110.3063	3.8117
MgMnH3	3.3199	36.58	−2721.18708	119.2684	3.6840
MgFeH3	3.2958	35.78	−2949.82054	123.0484	5.0208
MgCoH3	3.2997	35.93	−3191.19469	121.1560	4.2163
MgNiH3	3.3572	37.68	−3445.89536	113.8785	4.2121
MgCuH3	3.4817	42.20	−3714.17848	84.6760	4.0962

The variation in total energy as a function of volume allows us to identify the point of convergence corresponding to the fundamental state of the system, as illustrated in Figure 2.

Analysis of the total energy convergence point enables us to determine the optimum internal parameters for each $MgXH_3$ [49]. A series of optimization tests is carried out to refine the values of the lattice constants, which are then compared with experimental results and previous theoretical studies (see Table 1). The consistency of these values confirms the reliability of the density functional theory (DFT) calculations. The optimization parameters obtained form an essential basis for studying the electronic properties of perovskite hydrides. Indeed, a precise description of the crystal structure enables detailed electronic calculations, including analysis of the density of electronic states and the dispersion of energy bands. These results offer fundamental insights into the optical and electronic properties of the material, paving the way for potential applications in hydrogen storage and conversion.

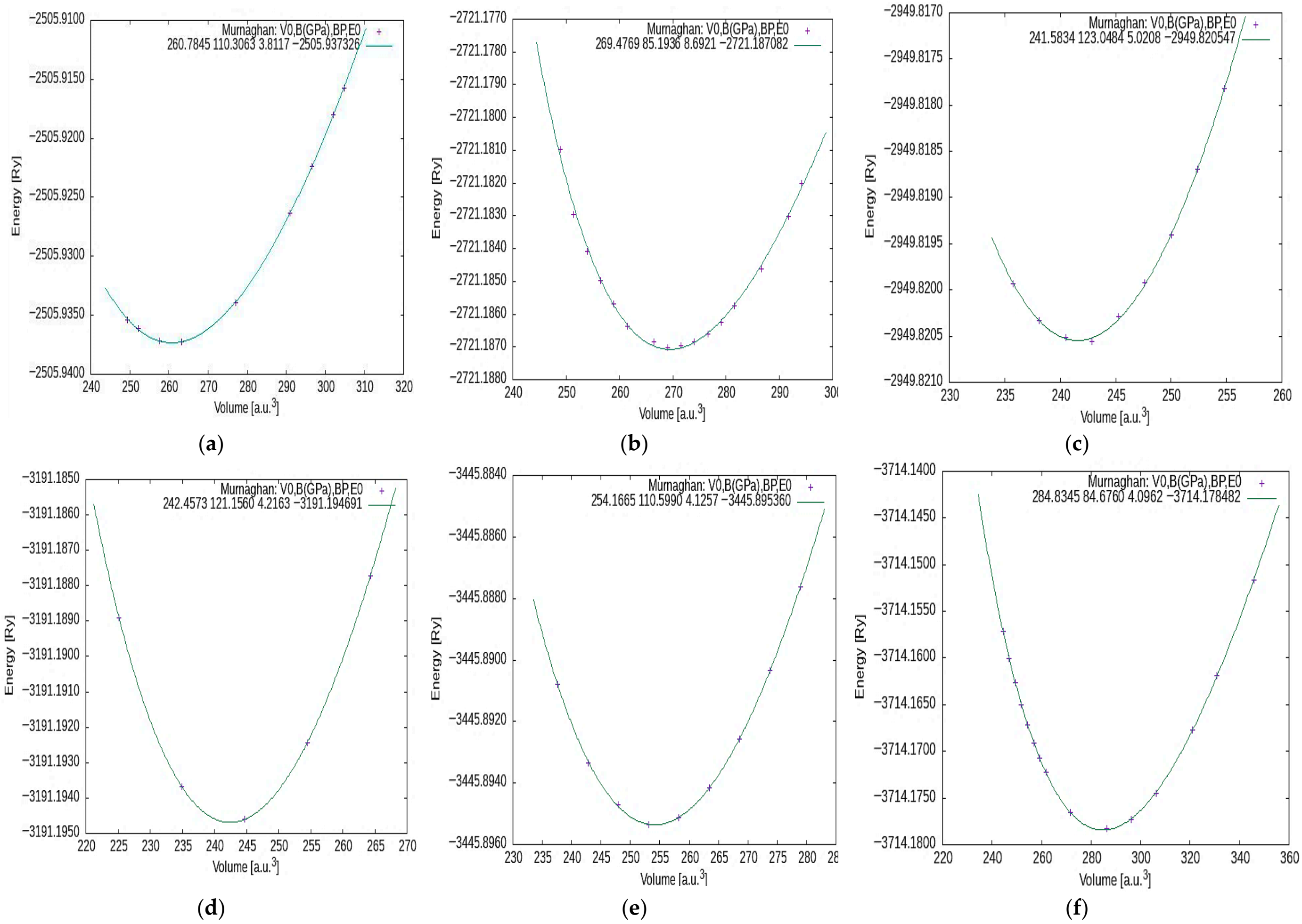

Figure 2. Variation of total energy for: (**a**) $MgCrH_3$, (**b**) $MgMnH_3$, (**c**) $MgFeH_3$, (**d**) $MgCoH_3$, (**e**) $MgNiH_3$ and (**f**) $MgCuH_3$.

Using the equation presented in Equation (2), the gravimetric hydrogen storage capacity of Mg*X*H_3 (X = Cr, Mn, Fe, Co, Ni, and Cu) perovskites was evaluated to determine their suitability for hydrogen storage applications. The gravimetric ratio (Cwt%) represents the amount of hydrogen stored relative to the total mass of the host perovskite material. This value is calculated as follows [50]:

$$C_{w\%} = \left(\frac{\frac{H}{M} m_H}{m_{Host} + \left(\frac{H}{M}\right) m_H} \times 100 \right) \% \tag{2}$$

In Equation (2), H/M denotes the hydrogen-to-host-atom ratio, m_h represents the molar mass of hydrogen, and M_{host} refers to the molar mass of the host material. The computed Cwt% values, which reflect the gravimetric hydrogen storage capacities of the Mg*X*H_3 compounds, are summarized in Table 3.

Table 3. The gravimetric and total energy values associated with the elements.

Element	Atomic Number	Gravimetric (Cwt%)	Total Energy E (Ry)
Cr	24	5.378	−2505.93726
Mn	25	5.111	−2721.18708
Fe	26	5.034	−2949.82054
Co	27	4.788	−3191.19469
Ni	28	4.607	−3445.89536
Cu	29	4.462	−3714.17848

Analysis of the data in Table 3 and Figure 3 highlights a clear trend: as the atomic number of element X in Mg*X*H_3 increases, both the gravimetric capacity and the total energy systematically decrease. This development can be attributed to the increase in atomic size and volume occupied by the transition element X, leading to a decrease in the mass-to-volume ratio and modifying the energetic stability of the crystal structure [51,52].

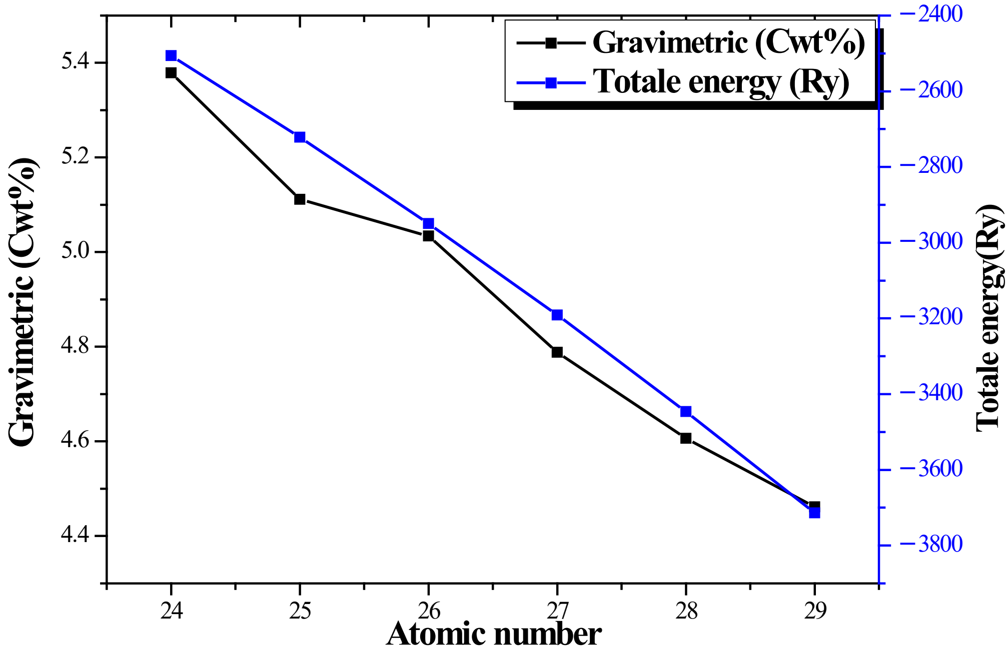

Figure 3. Gravimetric and Total energy of Mg*X*H_3.

Our calculated gravimetric hydrogen capacities for the Mg*X*H_3 series (5.37 wt% for $MgCrH_3$ down to 4.46 wt% for $MgCuH_3$) place these perovskite hydrides below the capacity of bulk MgH_2 (≈7.6 wt%), but within the range reported for other perovskite-type hydrides in the literature. MgH_2 remains the benchmark for maximum gravimetric density (~7.6 wt%) [53]. Studies on Mg*X*H_3-type perovskites report gravimetric values typically around 3.3–3.7 wt% for Ni/Cu/Co variants, so our values (4.46–5.37 wt%) are comparable or slightly higher depending on the precise composition and calculation conventions used [40].

In our study, we observed that the element Cr (atomic number 24) has a gravimetric capacity of 5.37% and a total energy of −2505.9436 Ry. Moving on to Mn (atomic number 25), the gravimetric capacity decreases to 5.11%, and total energy becomes more negative with a value of −2721.50432 Ry. This trend continues for the elements Fe (atomic number 26, and −2949.8248 Ry), Co (atomic number 27, 4.78% and −3191.19476 Ry), Ni (atomic number 28, 4.60% and −3445.8954 Ry), and finally Cu (atomic number 29, 4.46% and total energy −3714.17806 Ry). These results are in line with the fundamental principles of materials physics and quantum chemistry. Indeed, the energy required to form a cation from a neutral atom is influenced by several interdependent factors. These include atomic size (atomic radius), effective nuclear charge, and more complex quantum effects such as electronic shielding and d-orbital stabilization [54–56].

An increase in atomic number leads to an expansion of the electron cloud, which reduces the local electron density and alters the strength of chemical bonds in the $MgXH_3$ lattice. This results in a gradual decrease in gravimetric capacity and increased stabilization of the structure, as evidenced by lower total energy E values. Another consequence of this trend is its impact on the mechanical properties of the compounds studied. It appears that $MgCrH_3$ is the most ductile material among the perovskite hydrides studied, while $MgCuH_3$ exhibits greater rigidity. This observation correlates with variations in interatomic interactions and resistance to structural deformation induced by the valence orbital arrangement of transition metals. As such, these results provide valuable insights into materials engineering for specific applications, notably in hydrogen storage and energy devices. A thorough understanding of the relationships between electronic structure, thermal stability, and mechanical properties is essential to optimize the design of new functional materials based on hydride perovskites.

The volumetric and Mg-H distances for magnesium and hydrogen in $MgXH_3$ are numerical values given in Table 4. This data allows for the study of the interdependence of the chemical characteristics of the transition element X and the structural features of the associated perovskite hydrides.

Table 4. Values of volume and distance between Mg-H associated with elements.

Element	Atomic Number	Volume (Å^3)	Distance (Å)
Cr	24	38.67	3.38
Mn	25	36.58	3.32
Fe	26	35.78	3.29
Co	27	35.93	3.30
Ni	28	37.68	3.36
Cu	29	42.20	3.48

The distance between Mg and H changes with the atomic number of the transition element. For Cr to Fe, this distance generally decreases, then Co and Ni show more gradual increases, and a much more rapid increase is seen in Cu. At the same time, atomic volume shows a progressive decrease from Cr to Fe, followed by a slight rise for Co, and a dramatic increase for Ni and Cu. Multiple physical and chemical reasons cause the changes in Mg-H distances in perovskite hydrides. The atomic radius and electron density have the greatest contribution. The reduction in effective nuclear charge due to the increasing degree of contraction of d-orbitals from Cr to Fe leads to these distances being reduced. On the opposite side, for Ni and Cu, filling of d-orbitals results in expansion of atomic volume and an increase in interatomic distances. Moreover, the relevant bond ionicity and covalency of the transition elements also impact the charge distribution as well as the electronegativity and electron affinity, which changes the strength of Mg-H bonds and, as a result, their hydride stability. For Cu, larger Mg-H distances, which indicate lower structural stability, are generally observed, whereas a more stable and compact structure is seen in the case of Fe and Co, which explains why minimal distances are set for these two elements.

Figure 4 summarizes these trends by showing the relation of atomic numbers of the transition elements to their atomic volumes and Mg-H distances. This plot shows a general trend of contracting distances up to iron, followed by expansion for nickel and copper. The results discussed above yield an essential understanding of the observed variations in density and stability of perovskite hydrides and are indicative of their possible applications in advanced energy devices and hydrogen storage. Therefore, the analyses indicate that the structural and electronic properties of Mg$X$$H_3$ perovskite hydrides with the X variable in the position of the transition element X are a profound type within this range. Hence, grasping these asymmetries of structure is crucial for further developing innovative energy technologies and intelligent materials.

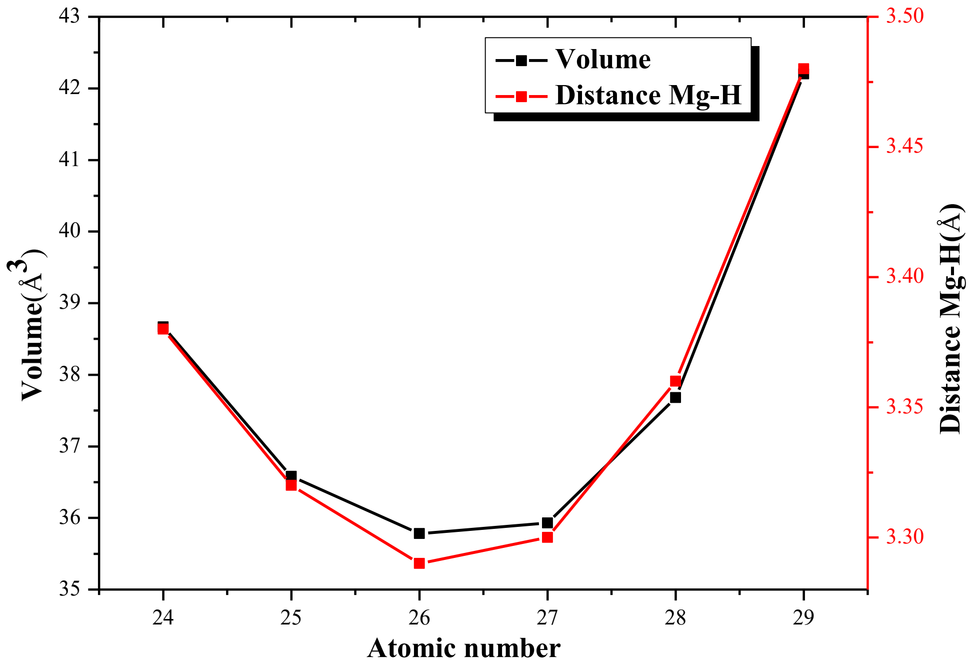

Figure 4. Volume and distance Mg-H for $MgXH_3$.

3.2. Electronic Properties

The electronic band structures of $MgXH_3$ magnesium hydrides are shown in Figure 5. A detailed analysis of these structures reveals an overlap between the conduction and valence bands, characteristic of pronounced metallic behavior for all the compounds studied [57]. This phenomenon is directly linked to the electronic stability of the hydrides, indicating a progressive decrease in their structural stability, resulting in a shift in electronic states towards the conduction bands [58]. This trend, observed through theoretical calculations, is in agreement with experimental results reported in the literature [59]. A detailed analysis of the atomic contributions to the electronic structure of $MgXH_3$ makes it possible to identify the role of each element in the formation of conduction and valence bands. Examination of Figure 5a reveals that $MgCrH_3$ exhibits notable contributions from Cr and hydrogen in the conduction band, while magnesium plays a prominent role in the valence band. Similarly, Figure 5b shows that manganese (Mn) is the main contributor to the conduction band in $MgMnH_3$, strongly influencing the compound's electronic properties. In the case of $MgFeH_3$, shown in Figure 5c, a significant contribution from iron and hydrogen is observed in the conduction band, while magnesium remains dominant in the valence band. Figure 5d illustrates that in $MgCoH_3$, cobalt plays an essential role in the conduction band. A similar evolution is observed for $MgNiH_3$, where nickel and hydrogen contribute strongly to the conduction band, while magnesium still dominates the valence band, as shown in Figure 5e. Finally, Figure 5f highlights that in $MgCuH_3$, copper and hydrogen actively participate in the conduction band, while magnesium retains a marked influence on the valence band [60–62]. These results underline a general trend in which magnesium remains a key player in the valence band, while transition atoms (Cr, Mn, Fe, Co, Ni, Cu) and hydrogen are predominantly involved in the conduction band [63]. This electronic distribution directly influences the metallic properties of the compounds and can be correlated with their stability and potential applications in catalysis and hydrogen storage.

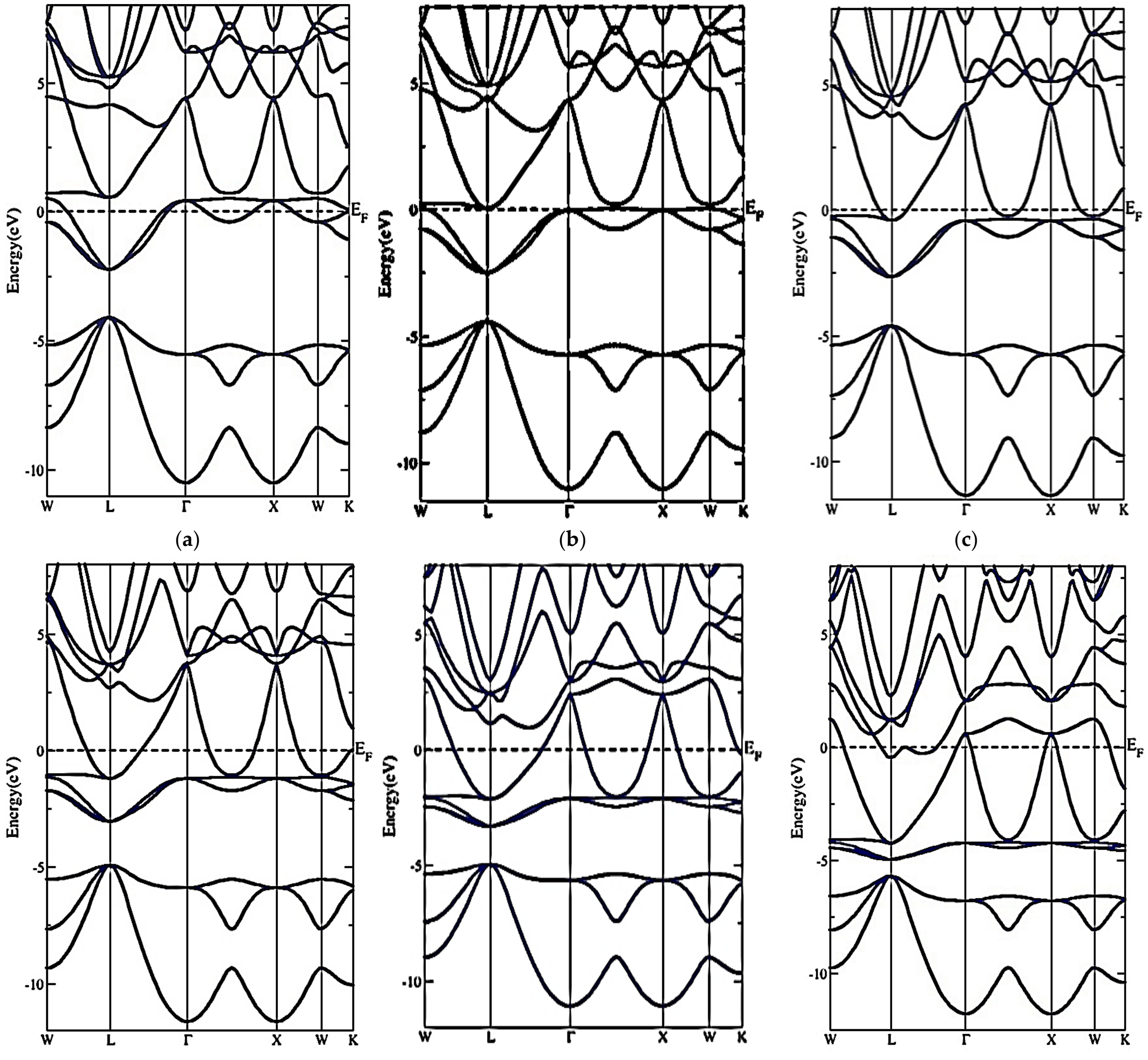

Figure 5. Band structures of (**a**) $MgCrH_3$, (**b**) $MgMnH_3$, (**c**) $MgFeH_3$, (**d**) $MgCoH_3$, (**e**) $MgNiH_3$ and (**f**) $MgCuH_3$.

The DOS analysis of Figure 6 aims to better understand the distribution of electronic states and to identify the specific contributions of atomic orbitals to the formation of conduction and valence bands. Figure 6 illustrates these results, highlighting the major influence of the Mg-s and H-s orbitals on the conduction band. The progressive evolution of intensity peaks towards higher energy levels indicates a decrease in the material's electronic stability [57,58,64]. To ensure a complete representation, an energy range from −10 to 7 eV was used for both TDOS and PDOS calculations. The PDOS study for $MgCrH_3$ (Figure 6a) reveals that the Cr-d and H-s orbitals play a dominant role in the conduction band. Chromium's contribution to the density of electronic states manifests itself mainly near the E_F, highlighting its impact on the material's conductivity. For $MgMnH_3$ (Figure 6b), a strong contribution from Mn-d orbitals is observed in the conduction band. This interaction between manganese and hydrogen modifies the electronic distribution and could influence the structural stability of the compound. Regarding $MgFeH_3$ (Figure 6c), the conduction band is dominated by Fe-d and H-s orbitals, whereas the Mg-s states are predominantly confined to the valence band. This electronic distribution is important in understanding charge transport mechanisms and cohesion of the material. Examination of $MgCoH_3$ (Figure 6d) reveals a non-zero density of states at EF, which verifies the metallic character of the compound. The most important electronic interactions are attributed to H-s, Co-d, and Mg-s, which may be relevant for the material's electrochemical properties. Similarly to $MgNiH_3$ (Figure 6e), the non-zero PDOS at the EF suggests the existence of a metallic behavior. The strong interaction between Ni-d and H-s orbitals indicates the electronic coupling between nickel and hydrogen, which affects the stability and transport properties of the material. Ultimately, $MgCuH_3$ (Figure 6f) has an electronic structure with Cu-d and H-s dominantly contributing within the conduction band, while Mg-s states are mostly confined in the valence band. This electronic configuration may rationalize the pronounced tendency to lower the structural stability of this compound. Overall, these results confirm that all the hydrides studied possess a metallic character, as indicated by the non-zero PDOS at E_F.

The distribution of electronic states, influenced by transition metal and hydrogen orbitals, plays a key role in the stability and electronic properties of these materials. These observations point the way to the optimization of perovskite hydrides for specific applications, notably in conductive and catalytic materials.

The metallic behavior predicted for all $MgXH_3$ compounds aligns with previous theoretical studies, although experimental verification remains limited. It is expected that synthesis conditions, point defects, or external pressure could slightly modify the band structure and induce semimetallic or narrow-gap characteristics.

3.3. Thermal Properties

The electronic band structure significantly affects how electron transport properties behave and is computed using stiff band theory and semi-classical Boltzmann transport theory as implemented in the Boltz-Trap package. For renewable energy systems, where thermal energy is frequently wasted in various energy-consuming processes, materials like $MgXH_3$ are essential [65]. We found that $MgXH_3$ exhibits significant thermoelectric properties based on power factor (PF), merit factor (Zt), electrical conductivity (σ), and thermal conductivity (κ). The thermally activated flow of free charge carriers has received relatively little attention in the existing literature. However, as in most materials, several factors may influence the electrical conductivity of $MgXH_3$ compounds. Variations in chemical composition across the sample, differences in crystal orientation, and the presence of defects or impurities can all affect charge transport behavior. Furthermore, since these parameters can strongly impact the electronic properties, the temperature and pressure conditions under which $MgXH_3$ is evaluated are also expected to influence its electrical conductivity.

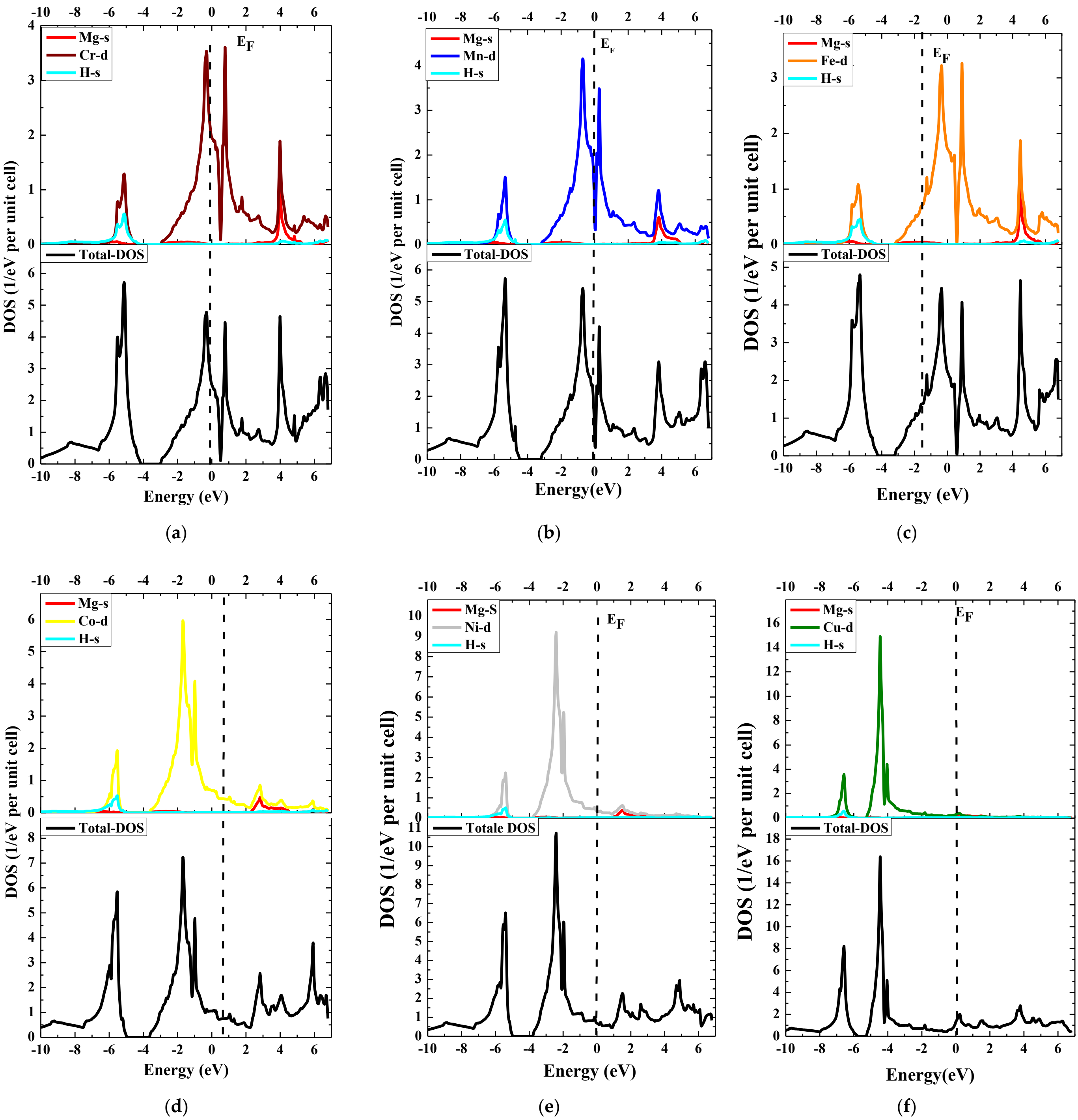

Figure 6. TDOS and PDOS: (**a**) $MgCrH_3$, (**b**) $MgMnH_3$, (**c**) $MgFeH_3$, (**d**) $MgCoH_3$, (**e**) $MgNiH_3$ and (**f**) $MgCuH_3$.

The electrical conductivity (σ) of $MgXH_3$ as a function of temperature is presented in Figure 7. The results reveal contrasting trends depending on the nature of the transition metal. Specifically, the conductivity of $MgNiH_3$ and $MgCuH_3$ decreases with increasing temperature, whereas for $MgCrH_3$, $MgMnH_3$, $MgFeH_3$, and $MgCoH_3$, σ increases gradually up to 900 K. At this temperature, the corresponding conductivity values are 2.50×10^6, 1.40×10^6, 7.40×10^5, 7.44×10^5, 7.50×10^5, and 7.52×10^5 $(1/(\Omega \cdot m))$ for $MgNiH_3$, $MgCuH_3$, $MgCrH_3$, $MgMnH_3$, $MgFeH_3$, and $MgCoH_3$, respectively. These results indicate that the type of transition metal plays a key role in determining the electrical response of the material with temperature.

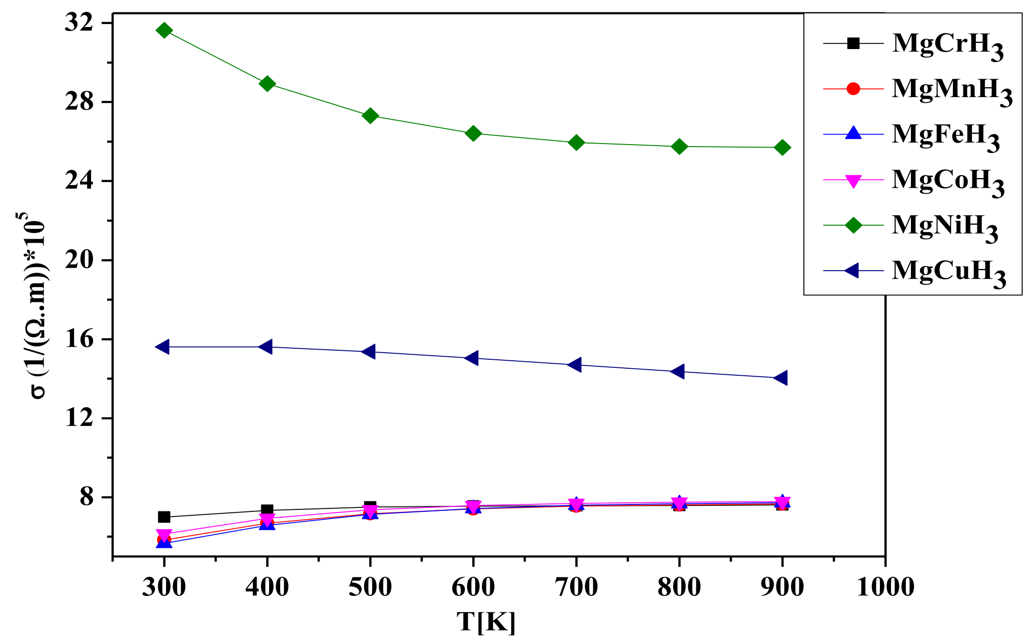

Figure 7. Electrical Conductivity of Mg*X*H_3.

For $MgNiH_3$ and $MgCuH_3$, the highest conductivity values, 3.45×10^6 and 1.53×10^6 $(1/(\Omega\cdot m))$, respectively, are observed at 300 K. The contrasting high-temperature behavior observed for $MgCrH_3$, $MgMnH_3$, $MgFeH_3$, and $MgCoH_3$ can be attributed to thermally activated carrier generation and enhanced carrier mobility with temperature. In these compounds, thermal excitation increases the number of free carriers and facilitates charge transport, resulting in semiconductor-like behavior. Conversely, $MgNiH_3$ and $MgCuH_3$ exhibit metallic characteristics, where increasing temperature leads to enhanced electron–phonon scattering and thus reduced carrier mobility, consistent with the conventional temperature dependence of electrical resistivity in metals and metallic alloys. Hence, this makes $MgNiH_3$ suitable as the most outstanding conducting agent needed for applications that require conduction at room temperature. In its turn, one could say $MgCuH_3$ is less competent but also effective. The variants of $MgCrH_3$, $MgMnH_3$, $MgFeH_3$, and $MgCoH_3$ that increase in conductivity with temperature can be applied in devices needing electronic performance at elevated temperatures. These results strongly support electronic structure and electron-phonon interactions in defining the electrical properties of transition metal-doped magnesium hydrides.

In Figure 8, the thermal conductivity (κ) of Mg$X$$H_3$ is plotted. An increase in κ with temperature is observed, reaching maximum values of 1.51×10, 1.505×10, 1.508×10, 1.512×10, 5.65×10, and 2.25×10 W/(K·m) for $MgCrH_3$, $MgMnH_3$, $MgFeH_3$, $MgCoH_3$, $MgNiH_3$, and $MgCuH_3$, respectively, corresponding to 900 K. The rate of heat transfer differs significantly between the compounds. Of all the hydrides studied, $MgCrH_3$ exhibits the lowest (κ), suggesting that there is less capability for heat transfer in this material. $MgNiH_3$ has, on the contrary, the highest κ, which indicates that this material is most efficient in heat transport. The contrast in κ is related to the different overall electronic and phononic interactions that govern heat propagation in the crystal lattice. The (κ) in these materials is predominantly dependent on the vibrations of free electrons and phonons inherent to the compound structure. When the temperature rises, molecular vibrations and phonon interaction become more intense, thus contributing to an enhancement of κ. Therefore, the linear rise observed is because of the maximum thermal excitation of heat carriers within the crystal lattice. In conclusion, the study of Mg$X$$H_3$ hydrides shows different thermal behavior with transition metals. $MgNiH_3$, with high (κ), may find its way into applications requiring efficient heat demolition, while $MgCrH_3$, with its low electrical conductivity, may be utilized as a thermal insulator. These findings highlight the importance of selecting materials for buildings based on thermal management requirements in various technological devices.

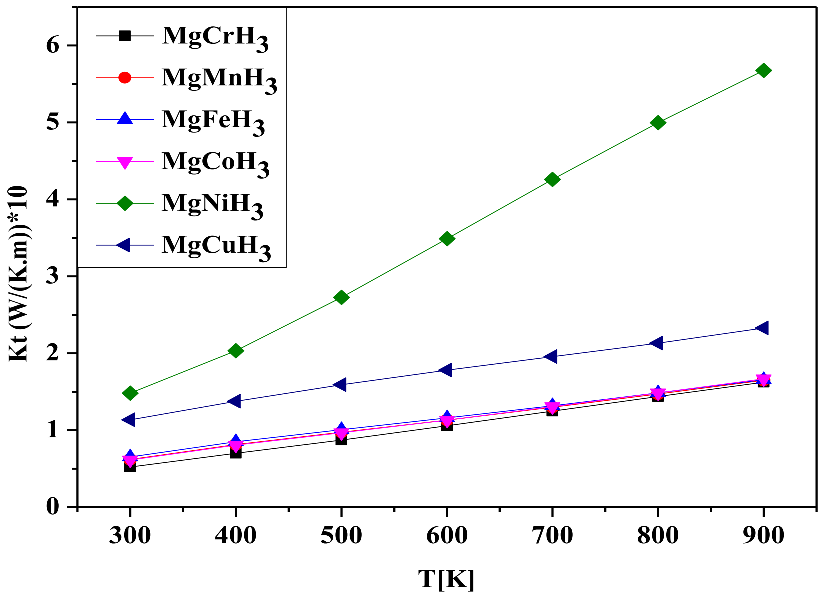

Figure 8. Thermal Conductivity of MgXH$_3$.

The Seebeck coefficient, thermal conductivity, and electrical resistivity are the factors that determine the dimensionless merit factor (Zt) of thermoelectric materials, which exploit temperature gradients to produce energy [66]. The following formula explains the merit factor (Zt):

The dimensionless thermoelectric figure of merit (Zt) is a key indicator of the performance of thermoelectric materials, which exploit temperature gradients to generate energy [65]. This factor is determined by three essential parameters: (S), (κ) and (σ). The mathematical relationship that describes Zt is given by the following equation [66]:

$$\mathbf{Zt} = \frac{\sigma s^2 T}{\kappa} \tag{3}$$

A material with high electrical conductivity, low thermal conductivity and a large Seebeck coefficient is more efficient for thermoelectric conversion, as it maximizes the potential difference induced by the thermal gradient. The evolution of Zt as a function of temperature is shown in Figure 9. Analysis of the results shows that, although Zt increases overall with temperature, it remains relatively low in all the compounds studied. This limitation is mainly attributed to the high thermal conductivity and suboptimal electrical behavior, characterized by a low density of electronic states at the E_F in the MgXH$_3$.

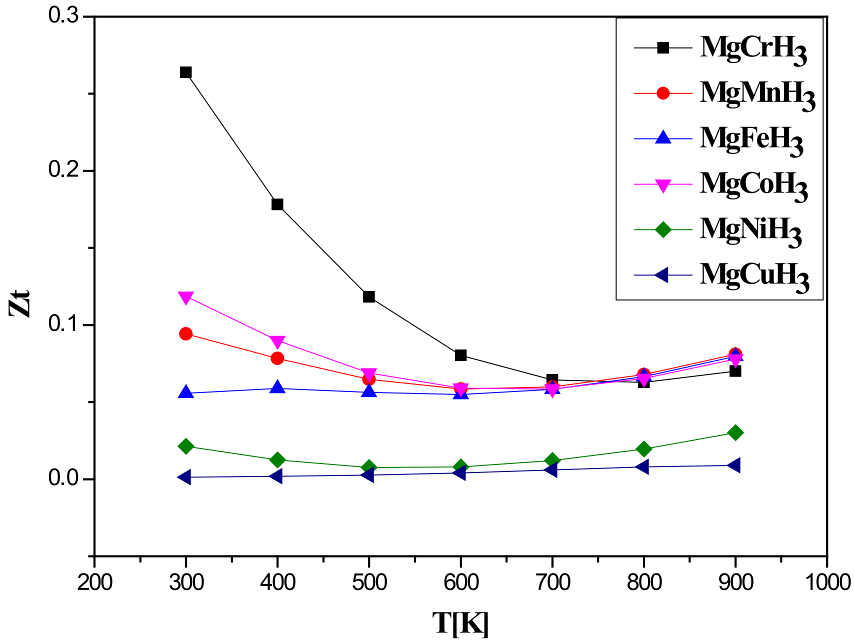

Figure 9. Merit factor of Mg*X*H_3.

Examining the specific trends, we observe a divergence in behavior between the different compounds. For $MgCrH_3$, $MgMnH_3$, and $MgCoH_3$, Zt decreases with increasing temperature, suggesting a progressive degradation of their thermoelectric properties at high temperatures. In contrast, $MgFeH_3$, $MgNiH_3$, and $MgCuH_3$ show an increase in Zt with temperature, reaching maximum values of 0.1, 0.115, 0.08, 0.12, 0.05, and 0.03, respectively, at 900 K. These results indicate that electronic and phononic interactions vary considerably depending on the transition metal involved in the Mg*X*H_3 structure. Furthermore, for $MgMnH_3$, $MgCoH_3$, and $MgCrH_3$, values of Zt were recorded at low temperatures (300 K), reaching 0.26, 0.117, and 0.098, respectively. This indicates that these materials are possibly suited for thermoelectric applications at low temperatures, while $MgFeH_3$, $MgNiH_3$, and $MgCuH_3$ perform better at high temperatures. Although the Zt values of $MgNiH_3$ and $MgCuH_3$ (0.12 and 0.05 at 900 K) remain below those of benchmark thermoelectrics such as Bi_2Te_3 and SnSe (typically ZT = 1) [67,68], these hydrides present a notable multifunctional potential combining hydrogen storage and moderate thermoelectric response. Further optimization with techniques such as doping or defect engineering could thus lead to improvements in their thermoelectric performance, through decreased thermal conductivity and tuning of electronic structure.

The efficiency of materials for thermoelectric devices is generally evaluated by the power factor (PF), which depends directly on the electrical conductivity (σ) and the Seebeck coefficient (S) according to the following equation:

$$\textbf{Power factor (PF)} = \sigma S^2 \quad (4)$$

A high-power factor is sought after, particularly for high-temperature applications where the exploitation of thermal gradients is essential for power generation. In this context, a material with a power factor greater than unity is considered promising for thermoelectric devices [65]. Figure 10 presents a graphical representation of the power factor (PF). It is observed that while the PF of $MgCrH_3$, $MgMnH_3$ and $MgCoH_3$ decreases with increasing temperature, that of $MgFeH_3$, $MgNiH_3$ and $MgCuH_3$ increases. At 900 K, these compounds reach values of 1.62×10^{-3}, 1.57×10^{-3}, 1.55×10^{-3}, 1.5×10^{-3}, 1.9×10^{-3} and 2.5×10^{-4} W/(K^2.m), respectively. While $MgFeH_3$, $MgNiH_3$ and $MgCuH_3$

has a lower temperature of 900 K, but the $MgFeH_3$, $MgNiH_3$ and $MgCuH_3$ has a lower temperature of 300 K, the material $MgCrH_3$, $MgMnH_3$ and $MgCoH_3$ have a very significant (PF) value of 3.23×10^{-3} W/K^2.m, 2.00×10^{-3} W/(K^2.m), and 2.4×10^{-3} W/(K^2.m) since its lowest temperature is 300 K. Furthermore, the presence of a high power factor for $MgNiH_3$ indicates that this material can convert thermal energy into electrical energy more efficiently. In contrast, the low values of PF for $MgCuH_3$ suggest a loss of thermal energy due to poor exploitation of the incoming power supply. Finally, it is important to point out that experimental and theoretical data on power factors for Mg$X$$H_3$ perovskites remain limited in the literature. These values can vary depending on several parameters, including chemical composition, temperature and sample purity. Future in-depth experimental and modeling studies are therefore needed to better understand and optimize the thermoelectric properties of these materials.

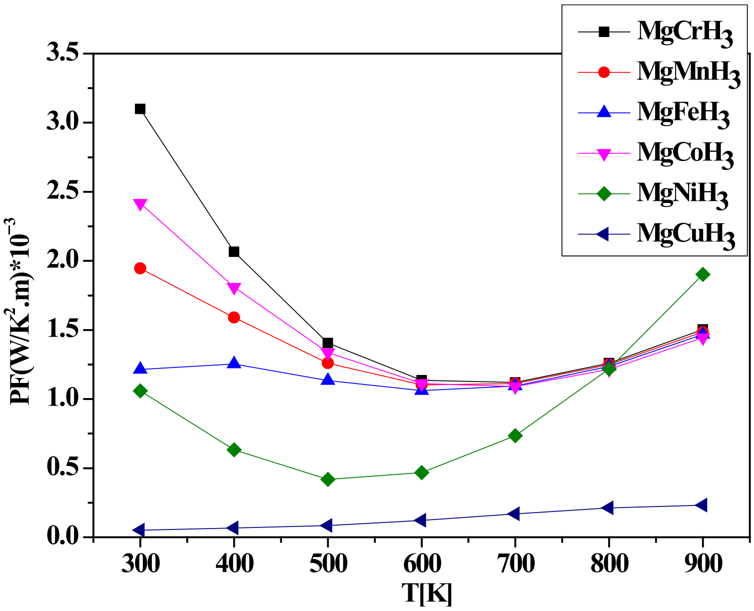

Figure 10. Power factor of Mg$X$$H_3$.

The electronic and thermal properties discussed in Sections 3.2 and 3.3 are closely related to hydrogen storage performance. The electronic band structure and DOS determine the strength and nature of Mg–H and X–H bonds, which directly influence hydrogen adsorption, desorption kinetics, and stability of the hydride lattice. Similarly, thermal conductivity and electrical transport behavior affect heat management during hydrogen absorption/desorption processes. Materials with moderate electrical conductivity and lower thermal conductivity, such as $MgCrH_3$ and $MgFeH_3$, ensure efficient hydrogen diffusion and thermal stability. Therefore, the thermoelectric analysis not only characterizes energy conversion potential but also provides key insight into the energetic and dynamic factors governing hydrogen storage efficiency in Mg$X$$H_3$ perovskites.

4. Conclusions

Analysis of electronic band structures reveals that these materials adopt a metallic behavior, characterized by an overlap between the conduction band and the valence band, leading to a zero electronic gap (Eg = 0 eV). DOS shows a strong contribution from transition metal orbitals near the E_F, influencing the electronic and thermal transport properties of the materials. The thermal properties of this family of Mg-based perovskites vary considerably depending on the transition metal involved. Our investigations have shown that the (κ) of the different materials increases with temperature, reaching its maximum values at 900 K, with $MgNiH_3$ exhibiting the highest κ and $MgCrH_3$ the lowest. Electrical conductivity (σ) follows a different evolution depending on the compounds: it decreases with temperature for $MgNiH_3$ and $MgCuH_3$, while it increases for the other materials ($MgCrH_3$, $MgMnH_3$, $MgFeH_3$ and $MgCoH_3$). The figure of merit (Zt) and power factor (PF) were analyzed to assess the thermoelectric potential of these materials. Our results indicate that $MgFeH_3$, $MgNiH_3$ and $MgCuH_3$ show relatively high performance at high temperatures, while $MgCrH_3$, $MgMnH_3$ and $MgCoH_3$ display lower Zt values, limiting their efficiency for energy conversion. Despite their relatively high (κ) and low density of electronic states, $MgNiH_3$ and $MgCuH_3$ exhibit notable thermoelectric potential and could be exploited in energy applications. These encouraging thermal properties support energy conversion technologies, waste heat recovery and solid-state cooling. In addition, magnesium-based perovskite hydrides are of particular interest for thermoelectricity and hydrogen storage.

Author Contributions: A.K.: Writing—original draft, Visualization, Validation, Investigation, Formal analysis, Data curation, Conceptualization. Y.Z.: Supervision. H.B.: Visualization, Validation, Formal analysis. All authors have read and agreed to the published version of the manuscript.

Funding: The authors are warmly grateful to "The Moroccan Association of Sciences and Techniques for Sustainable Development (MASTSD), Beni Mellal, Morocco" for the financial support.

Data Availability Statement: Data will be made available on request.

Conflicts of Interest: The authors declare that they have no known competing financial interests or personal relationships that could have appeared to influence the work reported in this paper.

References

1. Pan, Y.; Ende, Y. New insight into the structural and physical properties of AlH_3. *Energy Res.* **2022**, *46*, 19678–19685. [CrossRef]
2. Alonso, J.; Cabria, I.; Lopez, M. Simulation of hydrogen storage in porous carbons. *J. Mater. Res.* **2013**, *28*, 589–604. [CrossRef]
3. Ende, Y.; Pan, Y. Catalytic properties of borophene/MoS_2 heterojunctions for hydrogen evolution reaction under different stacking conditions. *J. Mater. Chem. A* **2022**, *46*, 24866–24876.
4. Pandey, P.; Shukla, S. Pandey Mesoporous silica beads encapsulated with functionalized palladium nanocrystallites: Novel catalyst for selective hydrogen evolution. *J. Mater. Res.* **2017**, *32*, 3574–3584. [CrossRef]
5. Sosa, A.N.; de Santiago, F.; Miranda, Á.; Trejo, A.; Salazar, F.; Pérez, L.A.; Cruz-Irisson, M. Alkali andtransition metal atom-functionalized germanene for hydrogen storage: A DFT investigation. *Int. J. Hydrogen Energy* **2020**, *46*, 20245–20256. [CrossRef]
6. Usman, M.R. Hydrogen storage methods: Review and current status. *Renew. Sustain. Energy Rev.* **2022**, *167*, 112743. [CrossRef]
7. Pan, Y.; Ende, Y. Theoretical prediction of structure, electronic and optical properties of VH2 hydrogen storage material. *Int. J. Hydrogen Energy* **2022**, *47*, 27608–27616. [CrossRef]
8. Laghlimi, C.; Moutcine, A.; Ziat, Y.; Belkhanchi, H.; Koufi, A.; Bouyassan, S. Hydrogen, Chronology and Electrochemical Production. *Sol. Energy Sustain. Dev.* **2024**, *14*, 22–37. [CrossRef]
9. Chen, S.; Pan, Y. Mechanism of interlayer spacing on catalytic properties of MoS_2 from ab-initio calculation. *Appl. Surf. Sci.* **2022**, *599*, 154041. [CrossRef]
10. Adaikalam, K.; Vikraman, D.; Karuppasamy, K.; Kim, H.S. Solar hydrogen production and storage in solid form: Prospects for materials and methods. *Nanomaterials* **2024**, *14*, 1560. [CrossRef]
11. Nagpal, M.; Kakkar, R. An evolving energy solution: Intermediate hydrogen storage. *Hydrog. Energy* **2018**, *43*, 12168–12188. [CrossRef]
12. Schlapbach, L.; Züttel, A. Hydrogen-storage materials for mobile applications. *Nature* **2001**, *414*, 353–358. [CrossRef]
13. Lim, K.; Kazemian, H.; Daud, Z.Y. Solid-state materials and methods for hydrogen storage: A critical review. *Chem. Eng. Technol.* **2010**, *33*, 213–226. [CrossRef]
14. Wu, Z.; Zhu, L.; Yang, F.; Nyamsi, S.; Porpatha, E. Toward the design of interstitial nonmetals co-doping for Mg-based hydrides as hydrogen storage material. *J. Mater. Res.* **2018**, *33*, 4080–4091. [CrossRef]
15. Batalovi, K.; Radakovi, C.; Belo, C.; Kotesk, V. Transition metal doping of Mg_2FeH_6—A DFT insight into synthesis and electronic structure. *Phys. Chem. Chem. Phys.* **2014**, *24*, 12356–12361. [CrossRef] [PubMed]
16. Baro, M.D.; Surinach, S.; Rossinyol, E.; Marini, A.; Girella, A.; Milanese, C.; Pellicer, E.; Garroni, S. Hydrogen sorption performance of MgH_2 doped with mesoporous nickeland cobalt-based oxides. *Int. J. Hydrogen Energy* **2011**, *36*, 540–5410.

17. Haider, S.; Haider, A.; Ud-Din Khan, S. (Eds.) *Density Functional Theory: New Perspectives and Applications*; IntechOpen: London, UK, 2024.
18. Khatun, S.; Bhagat, R.P.; Amin, S.A.; Jha, T.; Gayen, S. Density functional theory (DFT) studies in HDAC-based chemotherapeutics: Current findings, case studies and future perspectives. *Comput. Biol. Med.* **2024**, *175*, 108468. [CrossRef]
19. Feng, J.; Wan, L.; Li, J.; Jiao, S.; Cui, X.; Hu, W.; Yang, J. Massively parallel implementation of iterative eigensolvers in large-scale plane-wave density functional theory. *Comput. Phys. Commun.* **2024**, *299*, 109135. [CrossRef]
20. Raghavan, V. *Materials Science and Engineering: A First Course*; PHI Learning Pvt. Ltd.: Delhi, India, 2015.
21. Zhang, S.; Makoś, Z.; Jadrich, R.B.; Kraka, E.; Barros, K.; Nebgen, B.T.; Tretiak, S.; Isayev, O.; Lubbers, N.; Messerly, R.A.; et al. Exploring the frontiers of condensed-phase chemistry with a general reactive machine learning potential. *Nat. Chem.* **2024**, *16*, 727–734. [CrossRef]
22. Butera, V. Density functional theory methods applied to homogeneous and heterogeneous catalysis: A short review and a practical user guide. *Phys. Chem. Chem. Phys.* **2024**, *26*, 7950–7970. [CrossRef]
23. Cernatic, F.; Loos, P.F.; Senjean, B.; Fromager, E. Neutral electronic excitations and derivative discontinuities: An extended N-centered ensemble density functional theory perspective. *Phys. Rev. B* **2024**, *109*, 235113. [CrossRef]
24. Alvertis, A.M.; Williams-Young, D.B.; Bruneval, F.; Neaton, J.B. Influence of Electronic Correlations on Electron–Phonon Interactions of Molecular Systems with the GW and Coupled Cluster Methods. *J. Chem. Theory Comput.* **2024**, *20*, 6175–6183. [CrossRef] [PubMed]
25. Bosoni, E.; Beal, L.; Bercx, M.; Blaha, P.; Blügel, S.; Bröder, J.; Callsen, M.; Cottenier, S.; Degomme, A.; Dikan, V.; et al. How to verify the precision of density-functional-theory implementations via reproducible and universal workflows. *Nat. Rev. Phys.* **2024**, *6*, 45–58. [CrossRef]
26. Gusarov, S. Advances in Computational Methods for Modeling Photocatalytic Reactions: A Review of Recent Developments. *Materials* **2024**, *17*, 2119. [CrossRef]
27. Ribaldone, C.; Casassa, S. Born–Oppenheimer Molecular Dynamics with a Linear Combination of Atomic Orbitals and Hybrid Functionals for Condensed Matter Simulations Made Possible. Theory and Performance for the Microcanonical and Canonical, Ensembles. *J. Chem. Theory Comput.* **2024**, *20*, 3954–3975. [CrossRef] [PubMed]
28. Bouzaid, A.; Ziat, Y.; Belkhanchi, H.; Hamdani, H.; Koufi, A.; Miri, M.; Laghlimi, C.; Zarhri, Z. Ab initio study of the structural, electronic, and optical properties of $MgTiO_3$ perovskite materials doped with N and P. *E3S Web Conf.* **2024**, *582*, 02006. [CrossRef]
29. Koufi, A.; Ziat, Y.; Belkhanchi, H.; Bouzaid, A. DFT and BoltzTrap investigations on the thermal and structural characteristics of the perovskite $MgCuH_3$ and $MgCoH_3$. *Comput. Condens. Matter* **2025**, *42*, e01010. [CrossRef]
30. Koufi, A.; Ziat, Y.; Belkhanchi. Study of the Gravimetric, Electronic and Thermoelectric Properties of XAlH3 (X = Be, Na, K) as hydrogen storage perovskite using DFT and the BoltzTrap Software Package. *Sol. Energy Sustain. Dev. J.* **2024**, *14*, 53–66. [CrossRef]
31. Ikeda, K.; Kogure, Y.; Nakamori, Y.; Orimo, S. Reversible hydriding and dehydriding reactions of perovskite-type hydride $NaMgH_3$. *Scripta Mater.* **2005**, *53*, 319–322. [CrossRef]
32. Nunez, J.A. High-Pressure and High-Temperature Synthesis of Light Perovskite Hydrides for Hydrogen Storage. Ph.D. Thesis, University Grenoble Alpes, Saint-Martin-d'Hères, France, 2022.
33. Sato, T.; Noréus, D.; Takeshita, H.; Häussermann, U. Hydrides with the perovskite structure: General bonding and stability considerations and the new representative $CaNiH_3$. *J. Solid State Chem.* **2005**, *178*, 3381–3388. [CrossRef]
34. Ikeda, K.; Kato, S.; Ohoyama, K.; Nakamori, Y.; Takeshita, H.T.; Orimo, S. Formation of perovskite-type hydrides and thermal desorption processes in Ca–T–H (T = 3d transition metals). *Scripta Mater.* **2006**, *55*, 827–830. [CrossRef]
35. Sato, R.; Saitoh, H.; Endo, N.; Takagi, S.; Matsuo, M.; Aoki, K.; Orimo, S.I. Formation process of perovskite-type hydride $LiNiH_3$: In situ synchrotron radiation X-ray diffraction study. *Appl. Phys. Lett.* **2013**, *102*, 091901. [CrossRef]
36. Koufi, A.; Ziat, Y.; Belkhanchi, H.; Miri, M.; Lakouari, N.; Bougayr, E.H.; Baghli, F.Z. A computational study of the structural and thermal conduct of $MgCrH_3$ and $MgFeH_3$ perovskite-type hydrides: FP-LAPW and BoltzTraP insight. *E3S Web Conf.* **2024**, *582*, 02003. [CrossRef]
37. Ikeda, K.; Sato, T.; Orimo, S.I. Perovskite-type hydrides—Synthesis, structures and properties. *Int. J. Mater. Res.* **2008**, *99*, 471–479. [CrossRef]
38. Yalcin, B.G.; Salmankurt, B.; Duman, S. Investigation of structural, mechanical, electronic, optical, and dynamical properties of cubic $BaLiF_3$, $BaLiH_3$, and $SrLiH_3$. *Mater. Res. Express* **2016**, *3*, 036301. [CrossRef]
39. Blaha, P.; Schwarz, K.; Madsen, G.K.; Kvasnicka, D.; Luitz, J. wien2k. In *An Augmented Plane Wave+ Local Orbitals Program for Calculating Crystal Properties*; Vienna University of Technology: Vienna, Austria, 2001.
40. Rehman, Z.U.; Rehman, M.A.; Rehman, B.; Sikiru, S.; Qureshi, S.; Ali, E.M.; Awais, M.; Amjad, M.; Iqbal, I.; Rafique, A.; et al. Ab initio insight into the physical properties of $MgXH_3$ (X = Co, Cu, Ni) lead-free perovskite for hydrogen storage application. *Environ. Sci. Pollut. Res.* **2023**, *30*, 113889–113902. [CrossRef]

41. ur Rehman, Z.; Rehman, M.A.; Rehman, B.; Amjad, M.; Awais, M.; Iqbal, I.; Rafique, A. A DFT study of structural, electronic, mechanical, phonon, thermodynamic, and H_2 storage properties of lead-free perovskite hydride $MgXH_3$ (X = Cr, Fe, Mn). *J. Phys. Chem. Solids* **2024**, *186*, 111801. [CrossRef]
42. Abdellaoui, M.; Lakhal, M.; Benzidi, H.; Mounkachi, O.; Benyoussef, A.; El Kenz, A.; Loulidi, M. The hydrogen storage properties of Mg-intermetallic-hydrides by ab initio calculations and kinetic Monte Carlo simulations. *Int. J. Hydrogen Energy* **2020**, *45*, 11158–11166. [CrossRef]
43. Garara, M.; Benzidi, H.; Abdellaoui, M.; Lakhal, M.; Benyoussef, A.; Mounkachi, O.; Loulidi, M. Hydrogen storage properties of perovskite-type $MgCoH_3$ under strain effect. *Mater. Chem. Phys.* **2020**, *254*, 123417. [CrossRef]
44. Matara, S.F.; Al Alamc, A.F.; Ouainic, N. Hydrogen Insertion Effects on the Electronic Structure of Equiatomic MgNi Traced by ab initio Calculations. *Z. Für Naturforschung B* **2013**, *68*, 44–50. [CrossRef]
45. Selgin, A.; Iyigor, A. Structural, electronic, elastic and thermodynamic properties of hydrogen storage magnesium-based ternary hydrides. *Chem. Phys. Lett.* **2020**, *743*, 137184. [CrossRef]
46. Murnaghan, F.D. On the theory of the tension of an elastic cylinder. *Proc. Natl. Acad. Sci. USA* **1944**, *30*, 382–384. [CrossRef] [PubMed]
47. Miri, M.; Ziat, Y.; Belkhanchi, H.; Koufi, A.; El Kadi, Y.A. Modulating the Electronic and Optical Properties of $InGeF_3$ Perovskite under Pressure: A Computational Approach. *Eur. Phys. J. B* **2025**, *98*, 47. [CrossRef]
48. Vala, M.; Bhatt, M.; Pajtler, M.V.; Kansara, S.; Sonvane, Y. DFT Insights into 2D Yttrium Arsenide: Pioneering New Avenues in Optoelectronic Materials. *Nano* **2025**, *10*, 2650001. [CrossRef]
49. Raza, H.; Hamid, G. Murtaza Optoelectronic and thermal properties of $LiXH_3$ (X = Ba, Sr and Cs) for hydrogen storage materials: A first principle study. *Solid State Commun.* **2019**, *299*, 113659. [CrossRef]
50. Surucu, G.; Candan, A.; Gencer, A.; Isik, M. First-principle investigation for the hydrogen storage properties of $NaXH_3$ (X = Mn, Fe, Co) perovskite type hydrides. *Int. J. Hydrogen Energy* **2019**, *44*, 30218–30225. [CrossRef]
51. Ededet, E.; Louis, H.; Chukwu, U.G.; Magu, T.O.; Udo, A.E.; Adalikwu, S.A.; Adeyinka, A.S. Ab Initio Study of the Effects of d-Block Metal (Mn, Re, Tc) Encapsulation on the Electronic, Phonon, Thermodynamic, and Gravimetric, Hydrogen Capacity of $BaXH_4$ Hydride Perovskites. *J. Electron. Mater.* **2024**, *53*, 250–264. [CrossRef]
52. Raza, H.H.; Murtaza, G.; Razzaq, S.; Azam, A. Improving thermodynamic properties and desorption temperature in MgH_2 by doping Be: DFT study. *Mol. Simul.* **2023**, *49*, 497–508. [CrossRef]
53. Yang, X.; Li, W.; Zhang, J.; Hou, Q. Hydrogen storage performance of Mg/MgH_2 and its improvement measures: Research progress and trends. *Materials* **2023**, *16*, 1587. [CrossRef]
54. Cargioli, N. Standard Model Physics and Beyond in Low Energy Neutrino Scattering and Parity Violating Electron Interactions with Nuclei. Ph.D. Thesis, University of Cagliari, Cagliari, Italy, 2024.
55. Takabe, H. Physical of Warm Dense Matters. In *The Physics of Laser Plasmas and Applications-Volume 2: Fluid Models and Atomic Physics of Plasmas*; Springer International Publishing: Cham, Switzerland, 2024; pp. 397–450.
56. Diao, X. A Computational Study of Mixed Metal Oxides. Ph.D. Thesis, UCL (University College London), London, UK, 2024.
57. Pan, Y. First-principles investigation of structural stability, electronic and optical properties of suboxide (Zr_3O). *Mater. Sci. Eng. B* **2022**, *281*, 115746. [CrossRef]
58. Pan, Y. The influence of Ag and Cu on the electronic and optical properties of ZrO from first-principles calculations. *Mater. Sci. Semicond. Process.* **2021**, *135*, 106084. [CrossRef]
59. Candan, A.; Kurban, M. Electronic structure, elastic and phonon properties of perovskite-type hydrides $MgXH_3$ (X = Fe, Co) for hydrogen storage. *Solid State Commun.* **2018**, *281*, 38–43. [CrossRef]
60. Du, Y.; Xu, N.; Chen, S.; Chen, Y.; Song, R.; Luo, W.; Zhang, W. First-principles study of the hydrogen storage properties of hydride perovskites XCuH3 (X= K, Rb) for hydrogen storage applications. *Int. J. Hydrogen Energy* **2024**, *78*, 713–720. [CrossRef]
61. Rehman, M.A.; Rehman, Z.U.; Usman, M.; Hamad, A. The DFT study of the structural, hydrogen, electronic, mechanical, thermal, and optical properties of KXH_3 (X = Ca, Sc, Ti, Ni) perovskites for H_2 storage applications. *Struct. Chem.* **2024**, *36*, 235–248. [CrossRef]
62. Tang, T.; Tang, Y. First-principles investigations for the structural, optoelectronic and hydrogen storage properties of double perovskite $KNaMg_2F_{6-x}H_x$ and $KNaAe_2H_6$ (Ae = Be, Mg, Ca). *Int. J. Hydrogen Energy* **2024**, *61*, 13–24. [CrossRef]
63. Halais, W.T.; Doghmane, M.; Bouhlala, A.; Chettibi, S. Structural, magnetic, and optoelectronic properties of rock salt MgO co-doped with Eu-TM (TM = Cu, Ag, and Au) for spintronic and UV detector applications: SP-DFT investigations. *Mod. Phys. Lett. B* **2024**, *38*, 2450180. [CrossRef]
64. Pan, Y. Influence of N-vacancy on the electronic and optical properties of bulk GaN from first-principles investigations. *Int. J. Energy Res.* **2021**, *45*, 15512–15520. [CrossRef]
65. Yaseen, M.; Ambreen, H.; Mehmood, R.; Munawar, I.; Nessrin, A.; Alshahrani, T.; Noreen, S.; Laref, A. Investigation of optical and thermoelectric properties of $PbTiO_3$ under pressure. *Phys. B Condens. Matter* **2021**, *615*, 412857. [CrossRef]

66. Ding, C.-H.; Duan, Z.-F.; Ding, Z.-K.; Pan, H.; Wang, J.; Xiao, W.-H.; Liu, W.-P.; Li, Q.-Q.; Luo, N.-N.; Zeng, J. $XMoSiN_2$ (X = S, Se, Te): A novel 2D Janus semiconductor with ultra-high carrier mobility and excellent thermoelectric performance. *Europhys. Lett.* **2023**, *143*, 1. [CrossRef]
67. Azadparvar, M.; Rahnamaye Aliabad, H.A.; Özdemir, E.G. Optoelectronic and thermoelectric properties of Sb_2S_3 under hydrostatic pressure for energy conversion. *AIP Adv.* **2023**, *13*, 065218. [CrossRef]
68. Li, J.C.; Li, D.; Qin, X.Y.; Zhang, J. Enhanced thermoelectric performance of p-type SnSe doped with Zn. *Scr. Mater.* **2017**, *126*, 6–10. [CrossRef]